Study and Characterize Optical and Electronics Properties of Fe_3O_4-Bi_2O_3 Nanocomposite: Theoretical and Experimental Method

Tewodros Gizaw Tsegaye

School of Applied Natural Science

Department of Applied Physics

Office of Graduate studies

A Thesis Submitted to the Department of Applied Physics in Partial Fulfillment for the Requirement of the Degree of Master of Science in Condensed Matter Physics

June 2024
Adama, Ethiopia

Study and Characterize Optical and Electronics Properties of Fe_3O_4-Bi_2O_3 Nanocomposite: Theoretical and Experimental Method

Tewodros Gizaw Tsegaye

Advisor
Gashaw Beyene (Ph.D)

School of Applied Natural Science
Department of Applied Physics

Office of Graduate studies

A Thesis Submitted to the Department of Applied Physics in Partial Fulfillment for the Requirement of the Degree of Master of Science in Physics (Condensed Matter Physics)

June 2024
Adama, Ethiopia

Declaration

I hereby declare that this Master Thesis entitled “Study and Characterize Optical and Electronics Properties of Fe_3O_4-Bi_2O_3 Nanocomposite: Theoretical and Experimental Method” is my original work. That is, it has not been submitted for the award of any academic degree, diploma or certificate in any other university. All sources of materials that are used for this thesis have been duly acknowledged through citation.

_____	_____	_____
Name of student	Signature	Date

Recommendation of Advisor

I, the major advisor of this Thesis, hereby certify that we have read the revised version of the thesis entitled ‘‘Study and Characterize Optical and Electronics Properties of Fe_3O_4-Bi_2O_3 Nanocomposite: Theoretical and Experimental Method” prepared under our guidance by Tewodros Gizaw submitted in partial fulfillment of the requirements for the degree of Master’’ of Science in Physics (Condensed Material Physics). Therefore, I recommend the submission of revised version of the thesis to the department following the application procedures.

Major Advisor	Signature	Date
Co-advisor	Signature	Date

Approval Page for thesis proposal

We hereby certify that the recommendation and suggestion given by the thesis review committee are appropriately incorporated into the final thesis entitled ‘‘Study and Characterize Optical and Electronics Properties of Fe_3O_4-Bi_2O_3 Nanocomposite: Theoretical and Experimental Method’’ by Tewodros Gizaw Tsegaye.

Major Advisor	Signature	Date
Co-advisor	Signature	Date

Approval of board reviewers

We, the undersigned, members of the board of reviewers of the thesis open defense by Tewodros Gizaw Tsegaye have read and evaluated the thesis entitled ‘‘Study and Characterize Optical and Electronics Properties of Fe_3O_4-Bi_2O_3 Nanocomposite: Theoretical and Experimental Method’ and assessed the understanding of the candidate about the thesis research. This is, therefore, to certify that the thesis is accepted.

Submitted by	Signature	Date
Chairperson	Signature	Date
Examiner	Signature	Date

Final approval and acceptance of the thesis are contingent upon submission of its final copy to the Office of Postgraduate Studies (OPGS) through the Department Graduate Council (DGC) and School Graduate Committee (SGC).

Head of Department	Signature	Date
School Dean (SoANS)	Signature	Date
Office of Postgraduate Studies, Dean	Signature	Date

Acknowledgment

Mentorship has not only enhanced my technical skills but also helped me develop critical thinking abilities that will be valuable in future endeavors. In addition, I extend my appreciation to Gashaw Beyene (Ph.D) for creating a supportive environment where ideas were encouraged and nurtured. The open-door policy they maintained allowed fruitful discussions that greatly enriched my understanding of the subject matter. Lastly, I want to acknowledge Gashaw Beyene (Ph.D) unwavering belief in my potential. His encouragement during moments of self-doubt played a crucial role in pushing me beyond perceived limits and achieving personal growth. I am indebted to Gashaw Beyene (Ph.D) for his significant contributions towards making this thesis paper successful. It has been an honor working under his supervision.

Abstract

Nanocomposites have a vital role in different applications due to their novel properties .In this study, we used theoretical and experimental methods. In theoretical method, we studied polarizability, refractive index and optical absorbance of Bi_2O_3@Fe_3O_4 core-shell nanocomposite. In this part, two optical resonances are appeared due to two interference of the composite. The two resonances are varied based on the concentration of core or shell material. In experimental part, Bi_2O_3 -Fe_3O_4 composite nanostructures were synthesized using chemical and biological synthesize routes. The structural properties of the composite were performed using XRD spectroscopy. In this analysis, in both routes both materials are present in the composite. It was understood that Fe_3O_4 nanoparticles were decorated around Bi_2O_3 in the morphology of nanostructures. Energy band gaps of Bi_2O_3 -Fe_3O_4 nanocomposite structures were obtained from Photoluminescence. The band gap values of nanostructures were calculated to be in the range of 2.33-2.36 eV.

Table of Contents Page

List of figures

List of Abbreviations

Bi_2O_3.....Bismuth Oxide

CS…….Core-Shell

DF……dielectric function

Eg ……Band gap energy

Fe_3O_4.....Magnetite (ferric oxide)

NP ……..Nanoparticle

PL……Photoluminescence

SPR …….Surface Plasmon Resonance

XRD……X-ray diffraction

Chapter one

Introduction

1.1 Background of the Study

Significant applications of bismuth oxide in the fields such as microelectronics (Singh et al., 2010), sensor technology (Bera et al., 2010), optical coatings (Huang et al, 2001), transparent ceramic glass manufacturing (Johnson et al, 2001) have been discovered during the last years. The material is characterized by a large energy band-gap, high photoconductivity, high refractive index, dielectric permittivity and photoluminescence. During the growth of crystallites with different geometric shapes, various phases occur. Until now, five polymorphic forms of bismuth oxides were obtained: two stable polymorphs, namely α and δ phases (α -Bi_2O_3 is monoclinic, δ -Bi_2O_3 is face-centered cubic), and three metastable phases, i.e. β, γ and ω (β -Bi_2O_3 is tetragonal, γ -Bi_2O_3 is body-centered cubic, ω -Bi_2O_3 is triclinic) (Shen et al, 2013, Lawrie et al, 2012). For nanometric thicknesses, BiO is predominant phase, while in case of micronic films, α -Bi_2O_3 and Bi_2O_3 are the main phase components (Subramanian et al, 2003).

Bismuth oxide nanoparticle (BONP) manufactured in different morphology used for different application s, for instant, for coating and heterojunction purpose, biological, medical, cosmetic and environmental remediation. Specially, sheet like (1D) structure of this material is very important for different applications and it broadly studied.

Thin films of bismuth oxides have been obtained using such methods as electro deposition, Bi_2O_3 1D nanostructures are quite sensitive to low concentrations of NO_2 in ambient air but are almost insensitive to most other common gasses (Liu et al, 2013). Nevertheless, enhancing their sensing performance and detection limits remains a challenge. Several techniques, such as surface functionalization (Kalele et al, 2006, Chavez et al, 2016, Lee et al,2011), doping (Carney, 2017, Lin et al, 2006, Beyene et al, 2019), core–shell structure formation (Kaminskiene et al, 2013, Link et al, 2000, Chen et al, 2014) and UV irradiation (Serhan et al, 2019, Shivola, 2000, Arkhipova et al, 2015), have been developed to enhance the sensing performance, detection limit and operation temperature of 1D nanostructure sensors. On the other hand, the effects of a combination of two of these techniques on the sensing properties of Bi_2O_3 1D nanostructure sensors have not been reported. In this study, multiple networked Bi_2O_3-core/ZnO-shell nano belt sensors were fabricated and their NO_2 gas sensing properties under UV illumination were examined to determine the combinational effects of core–shell structure formation and UV irradiation on the gas sensing properties of Bi_2O_3 1D nanostructures.

Among the various inorganic semiconductor nanomaterials, magnetite (Fe_3O_4) nanoparticles have attracted great attention due to the promising combination of size dependent electronic, optical, photochemical, and luminescent properties combined with the availability, a great variety of attainable geometries of nano-assemblies, and low toxicity (A.R. bijanzadeh, 2012). The broad spectrum of applications of Fe_3O_4 NPs, such as sensors, solar cells, bioimaging, photocatalysis, UV-shielding, LEDs put forth rigorous requirements for chemical, thermal, and photochemical stability of Fe_3O_4 NPs, versatility of surface chemistry, control of the Fe_3O_4 NP size and compatibility of Fe_3O_4 NPs with water based bio-environments.

In this work, we have studied the optical properties of spherical $Fe_3O_4@Bi_2O_3$ core-shell nanocomposite embedded in sodium dichromate medium using Mathematica Wolfram software.

There is an investigation on the optical properties and applications of noble magnetic@semiconductor core-shell nanocomposite (Wolf et al, 2014), however, to the best of our knowledge, investigation of plasmonic effect on optical properties of spherical $Fe_3O_4@Bi_2O_3$ core-shell nanocomposite is not yet reported. The host medium sodium dichromate ($Na_2Cr_2O_7$) used to protect corrosion, it is environmental friendship, it is not react with shell material. A single nanoparticles have a drawback for a certain or appropriate applications; hence modification or generate new properties for the desired applications it should be combined with other noble materials. By considering the noble properties and potential/versatile applications into account, the efforts are being made for optical properties of Fe_3O_4 and Bi_2O_3 by combining them using coating technique. Rather, these materials have been investigated most extensively because of their high catalytic, universal bio-compatibility, optical sensitivity, facile preparation, resistance to oxidation, and surface plasmon resonance (SPR) band that can absorb and scatter visible light relative to other noble metals (Sagadevan et al, 2017). We have seen the effect of shell thickness and core size on polarization, refractive index and optical absorption for new model of composite.

Experimentally, we synthesize the composite of ferric oxide with bismuth oxide with different morphology. As we stated above, these two materials have noble properties, so they will have enhanced properties. As already known, if the materials modified or enhanced properties, they will use for different fields. As far as our knowledge concern, there is no nanocompoiste made from these two materials.

The thesis is organized as follow: In chapter 2, we review some documents which are related with our work. Theoretical description of quantum dot $Fe_3O_4@Bi_2O_3$ core-shell nanocomposite is carried out using the electrostatic approximation and experimental work of this work in composite form is addressed in chapter 3. Numerical analysis and experimental results analysis are presented in chapter 4. Finally, in chapter 5 concluding remarks are given.

1.2 Statement of the Problem

Bismuth oxide (Bi_2O_3) and magnetite (Fe_3O_4) have a novel properties and wide applications but, the combination these two very important materials is not studied. Their

combination may have enhanced properties and used different applications. The morphology and the way of combination may have different applications. In this study, we try to combine and investigate the properties in theoretical and experimental method.

1.3 Significant of the Study

Significant applications of bismuth oxides in the fields such as microelectronics, sensor technology, optical coatings, transparent ceramic glass manufacturing has been discovered during the last years. The material is characterized by a large energy band-gap, high photoconductivity, high refractive index, dielectric permittivity and photoluminescence. Magnetite also has different morphology and different application too.

The study of these combination will use as frame for further investigation. Researchers and students may study in different morphology and combination for various applications.

1.4 Objective

1.4.1 General Objective

The general objective of this work is to study and characterize optical and electronics properties of Fe_3O_4-Bi_2O_3 nanocomposite using theoretical and experimental method.

1.4.2 Specific Objective

The specific objectives are:

- ⇒ To study polarizability, refractive index, and optical absorbance of the nanoinclusion embedded in non-absorptive host medium.
- ⇒ To investigate the effect of core and shell concentration and permittivity of the medium on the optical response.
- ⇒ To synthesize and characterize Fe_3O_4-Bi_2O_3 nanocomposite.
- ⇒ To compare the result of green and chemical synthesis of Fe_3O_4-Bi_2O_3 nanocomposite.

Chapter Two

2. Review of Related Literature

A great attention has been given to the development of nanomaterials as they exhibit unique material properties as compared to their bulk counterpart. These unique properties include optical, magnetic, specific heat, melting point, surface activities, chemical and biological properties (Wang et al, 2017). Nanomaterials forms heterogeneous structures composed of a noble magnetic and a semiconductor. These peculiar type of systems offers to design materials with novel and unique physical and chemical properties. As isolated systems, the optical properties of semiconductor quantum dots (QDs) and noble magnetic nanoparticles (NPs) are characterized by excitation of electron. In both cases, the required wavelengths to produce such excitations are governed mainly by the nanoparticle nature, size, shape, and local environment (Encina et al, 2013).

As an important class of nanomaterials, core-shell nanoparticles (CSNPs) that integrate two dissimilar materials with distinct functionalities have attracting more and more attention, since they have emerged at the frontier between materials chemistry and many other fields, such as biomedical, optics, catalysis and security purpose. Because core-shell NPs enable the synergistic coupling of the two constituents, they could offer the modified properties by changing either the constituting materials or the core to shell ratio. Therefore, this nanostructure can meet the diverse application requirements. Among various core-shell NPs, magnetic/semiconductor hybrid NPs have been studied as they possess intriguing magnetic/plasmonic and magnetic/catalytic properties, and they can be used in many fields, for example optical devices, chemical reactions as magnetically recyclable catalysts, bio imaging, targeted drug delivery. Fe_3O_4-based magnetic hybrid NPs play an important role in specialty chemistry, physics and material science. By varying the size of the Bi_2O_3 cores and Fe_3O_4 shell, the optical properties of nano hybrids can be tuned in a broad spectral range.

Magnetic/plasmonic nanostructures demonstrate multiple properties not present in individual nanomaterials. Such materials offer the advantage of being manipulated by an external magnetic field, showing tunable optical properties being adjustable in accordance with modifying shell thickness. Experimental and computational studies show that the higher the magnetization in magnetic nanoparticles, the more is the suitable response toward the exposed magnetic/electric field and the higher the effectiveness in nano medical diagnostics. Magnetic/plasmonic core shell possess dual magnetic and plasmonic properties and have wide spread applications in biomedical fields. The magnetic shells, such as Fe_3O_4 are greatly desired for applications such as magnetic separation, magnetic resonance imaging or magnetic guided drug delivery. The BO-cores can be chemically stabilized by coating them with metal oxides, which not only provides a chemically inert surface, but also introduces interesting plasmonic properties which can be utilized for sensing, imaging, and photo thermal therapy (Shankar, 2017).

The possibility of building new nanostructures by mixing Fe_3O_4 and Bi_2O_3 nanoparticles (NPs) opens up a wide spectrum of desirable synergistic and complementary effects. One of the challenges is the conjunction of these two dissimilar materials in a controlled way. Thus, great efforts have been made on synthetic routes to command the bonding of the hetero particle. The optical resonance at a certain wavelength of light optical polarization, dielectric function of the material and refractive of core-shell are affected by shell thickness, core size, electronic properties of shell and surrounding environment. This response and resonance mainly takes place at two interfaces; at outer interface between shell surface and host medium, and inner interface between shell and core semiconductor material. Localized surface plasmon resonance gives rise to an enhancement of electric field, localization of energy at nanometer scale, and strongly enhanced absorption and scattering of light.

Magnetic nanoparticles with a core-shell structure promises for many applications due to their multi functionality including optical, electronic, and magnetic properties. In particular, these Fe_3O_4@Bi_2O_3 core-shell NPs combine the magnetic and optical properties of Fe_3O_4 and Bi_2O_3 together, exhibiting great potential in the fields of bio-related separation, ultrasensitive detection and cellular imaging. Fe_3O_4 is one of the magnetic nanoparticles. Different reports are demonstrating that magnetic Fe_3O_4 can be used for waste water purification, such as to adsorb arsenite, arsenate, cadmium, nickel used to remove alkalinity and hardness, desalination, decolourization of pulp mill effluent and removal of natural organic compounds. After adsorption, Fe_3O_4 can be separated from the medium by a simple magnetic process.

Bismuth oxide (Bi_2O_3) is one of p-type semiconductor materials that have many excellent physical properties. Bi_2O_3 can be used as sensors (Sigh et al, 2010, Bera et al, 2010, Huang et al, 2001, Johnson et al, 2001), solid electrolyte in solid fuel cells (Sigh et al, 2010, Bera et al, 2010, Huang et al, 2001) and photocatalysts (Rakkesh et al, 2012). Owing to its unique chemical and physical properties such as high-energy band gap, high refractive index, high dielectric permittivity, and excellent photoconductivity, Bi_2O_3 has been the focus of scientific research (Ali et al, 2016). Several methods including sol–gel, flame spray pyrolysis, micro emulsion, hydrothermal, metal organic chemical vapour deposition process, vapour phase deposition technique, electro spinning technique, microwave-assisted heating method have been successfully used for the fabrication of Bi_2O_3 with different morphology. Bi_2O_3 needles have been prepared using $Bi(NO_3)_3$ as the precursor and NaOH as a precipitating agent under a required thermal treatment of 450°C for 4h (Subramanian). As reported in (Liu et al, 2013), a low-temperature synthesizing of α-phase Bi_2O_3 at 60°C and the products exhibit a flower-like architecture structure assembled by Bi_2O_3 micro-rods. Rod-like α-Bi_2O_3 and tetrahedral γ-Bi_2O_3 particles have been controlled fabricated by a facile solution crystallization method (Liu et al, 2015). Using different surfactants such as oleic acid (Johnson et al, 2001), dodecylbenzene sulfonate (Liu et al, 2017), sodium ethylene glycol (Kalele et al, 2006), and polyethylene glycol (Chavez et al, 2016), other researchers have controlled the morphologies

of Bi_2O_3 crystals with needle-like, flower-like or tetrahedral morphologies successfully. The researchers have discussed the important effect of above surfactants on the morphology of Bi_2O_3 products in detail. As far as we know, there are no reports about controlling the morphology of Bi_2O_3 products by heating ways. This letter aims to investigate the effect of Bi_2O_3 morphology through different ways of heating by a low-temperature liquid phase method. The Bi_2O_3 powders attained at 90°C possess a perfect tetrahedral and platelet shapes with a band gap of 3.0 eV. With their novel morphology and high-energy band gap, Bi_2O_3 powders have the potential to be applied to ultraviolet visible-light-driven photo catalyst for environmental cleanup and optoelectric devices for solar energy conversion to electricity.

Bismuth oxide (Bi_2O_3) is an important wide band gap semiconductor with four main crystallographic polymorphs denoted as α-, β-, γ-, and δ-Bi_2O_3 (Singh et al, 2010). Of these polymorphs, α- and δ-Bi_2O_3 are p-type semiconductors, whereas β-Bi_2O_3 is an n-type semiconductor. Owing to its unique physical properties, such as a large energy band gap, high refractive index, dielectric permittivity and high oxygen conductivity, as well as its remarkable photoconductivity and photoluminescence (Bera et al, 2010, Huang et al, 2001, Johnson et al, 2001), Bi_2O_3 has been studied extensively for a range of applications, such as gas sensors, photovoltaic cells, optical coatings, fuel cells, supercapacitors and photocatalysts (Singh et al, 2010, Rakkesh et al, 2012). Regarding gas sensor applications, one-dimensional (1D) nanostructures are expected to show a considerably enhanced performance because of their ultra-high surface-to-volume ratios and Debye length comparable to their dimensions, which makes their electrical properties extremely sensitive to surface-adsorbed species. Bismuth oxide 1D nanostructures have been prepared using a range of techniques such as metal–organic chemical vapor deposition, chemical methods (Ali et al, 2016), oxidative metal vapor transport deposition techniques (Subramanian et al, 2003), solution chemical methods (Liu et al, 2013), and stress-induced methods (Liu et al, 2015). On the other hand, the use of the vapor–liquid–solid (VLS) method to synthesize Bi_2O_3 1D nanostructures, has not been reported, despite it being most successful in generating 1D nanostructures with single crystalline structures and in relatively large quantities (Liu et al, 2017).

Fe_3O_4 nanoparticles have good electron affinity with outstanding magnetic and electronic properties. Such electronic properties enable them to be used in catalytic applications as magnetic catalyzers (Kurnaz et al). Iron oxide nanoparticles exhibit super paramagnetic and ferromagnetic properties; the magnetic characteristics of the nanoparticles may alter depending on their size. Iron oxide nanoparticles may find applications in different fields such as water purifications, catalysis, bio labeling, etc. Such magnetic properties help Fe3O4 nanoparticles to be used in magnetic resonance imaging (MRI) applications (Aslan et al). It was previously reported that Fe3O4 nanoparticles can be used as magnetic resonance imaging contrast agent. It was also evidenced in the literature that Fe3O4 nanoparticles can be used in magnetic hyperthermia applications. Fe_3O_4 nanoparticles are response to externally applied magnetic field. Application of the magnetic field in altering ways vibrates the nanoparticles.

Then, the temperature of the nanoparticles starts to increase. Increased temperature is able to kill the cancerous tissues around them. In the imaging process, MRI device continuously applies magnetic field to the region where imaging is performed. Applications of Fe3O4 nanoparticles before imaging both help to enhance the contrast of the MR image and can increase the temperature of the imaging region. Hence, increased temperature diminishes and/or kills the cancerous tissues in the area where MR imaging is performed. The material which can simultaneously be used in diagnostic and therapeutic applications is called theranostic material. In this regard, Fe3O4 nanoparticles have potential to be used in theranostic applications where both therapeutic and diagnostic (imaging) properties of the nanoparticles can be used simultaneously. Various parameters can measure the theranostic performance of the theranostic properties of the materials. For example, size can be an important factor, since change in the materials size can alter the magnetic characteristics of the materials. The changing in the magnetic performance can alter the magnetic hyperthermia properties and/or MRI weighting properties where augmented or decreased hyperthermia or contrast enhancement performance can be seen (Aslan et al).

Chapter Three

3. Material and Method

3.1 Numerical Method

Consider a spherical core-shell nanocomposite consisting of a semiconductor core of dielectric function (DF) $\mathfrak{E}_1$ and magnetic material shell of DF $\mathfrak{E}_2$ embedded in a dielectric host matrix, as shown in Fig. 3.1 The host medium is assumed to be isotropic and non-absorbing with dielectric constant ε_h. The parameters r_1 and r_2 are the radii of the core and core-shell composite, respectively. When an electromagnetic wave is incident on the core-shell nanocomposite, electric field is induced in the system due to polarization. For NPs of sizes (diameter = $2r_2$) much smaller than the wavelength of the incident light, the distribution of the electrostatic potential associated with the induced field can be obtained by solving the Laplace equation, $\nabla^2\Phi = 0$.

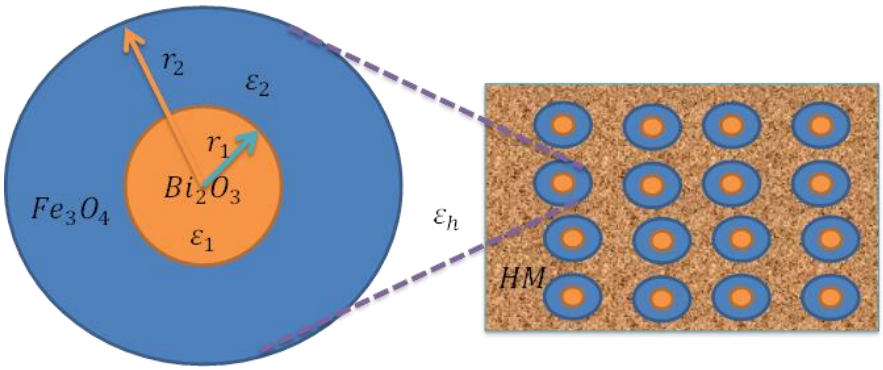

FIG. 3.1: The schematic diagram of a core-shell spherical nano inclusion embedded in host medium.

Suppose a uniform, static electromagnetic field polarized along the z-axis is applied on the spherical core-shell NP embedded in non-absorptive a host matrix. If the center of the NP is assumed to coincide with the origin of a spherical co-ordinate system, then the distribution of the potentials in the system may be found to be,

$$\Phi_1(r,\theta) = A_1 r\cos\theta, \qquad r < r_1 \qquad (3.1)$$

$$\Phi_2(r,\theta) = \left(A_2 r + \frac{B_1}{r^2}\right)\cos\theta, \qquad r_1 < r < r_2 \qquad (3.2)$$

$$\Phi_3(r,\theta) = \left(A_3 r + \frac{B_2}{r^2}\right)\cos\theta, \qquad r > r_2 \qquad (3.3)$$

where Φ_1, Φ_2 and Φ_3 are the potentials in the dielectric core, shell material, and host matrix, respectively, A_3 is a quantity associated with the external applied field, r is the distance from the center of the nanocomposite, θ is the zenith angle, and the coefficients A_1, A_2, B_1, B_2 are constants to be determined by using the appropriate boundary conditions at the interfaces.

It is worthwhile to note that the second term on the right-side of Eq. *(3.3)* represents the induced potential outside the core-shell nanocomposite. The optical properties of the system may readily described by the induced field out-side the concentric spheres. Consequently, it is suffice to determine the value of the coefficient B_2. Imposing the relevant boundary conditions in Eqs. (3.1) - (3.3), we obtain the following relation:

$$B_2 = \left[\frac{(\varepsilon_1 + 2\varepsilon_2)(\varepsilon_2 - \varepsilon_h) + v_f(\varepsilon_1 - \varepsilon_2)(2\varepsilon_2 + \varepsilon_h)}{(\varepsilon_1 + 2\varepsilon_2)(\varepsilon_2 + 2\varepsilon_h) + 2v_f(\varepsilon_1 - \varepsilon_2)(\varepsilon_2 - \varepsilon_h)}\right] A_3 r_2^3. \quad (3.4)$$

In view of Eq. (3.3), the induced potential outside the concentric spheres is then given by

$$\Phi_{ind} = \left(\frac{B_2}{r^2}\right) cos\theta. \quad (3.5)$$

Moreover, employing the dipole approximation, induced potential may also be expressed as (Ali et al,2016)

$$\Phi_{ind} = \frac{pcos\theta}{4\pi\varepsilon_h r^2}, \quad (3.6)$$

where p is the magnitude of the electric dipole moment of the system. In view of Eqs. (3.5) and (3.6), the dipole moment becomes

$$p = 4\pi\varepsilon_h B_2 = \varepsilon_h \alpha A_3, \quad (3.7)$$

where α is the polarizability of the composite given by

$$\alpha = 4\pi\left[\frac{(\varepsilon_1 + 2\varepsilon_2)(\varepsilon_2 - \varepsilon_h) + v_f(\varepsilon_1 - \varepsilon_2)(2\varepsilon_2 + \varepsilon_h)}{(\varepsilon_1 + 2\varepsilon_2)(\varepsilon_2 + 2\varepsilon_h) + 2v_f(\varepsilon_1 - \varepsilon_2)(\varepsilon_2 - \varepsilon_h)}\right] r_2^3, \quad (3.8)$$

Further, the polarizability of an equivalent sphere of effective DF ε_I embedded in a host matrix of DF ε_h can be expressed in form of the Clausius-Mossotti relation (Subramanian et al, 2003). That is,

$$\alpha = 4\pi r_2^3 \frac{\varepsilon_I - \varepsilon_h}{\varepsilon_I + 2\varepsilon_h}. \quad (3.9)$$

Equating Eqs. (3.8) and (3.9), we get the effective DF of the core-shell spherical inclusion to be

$$\varepsilon_I = \varepsilon_2 \frac{(\varepsilon_1 + 2\varepsilon_2) + 2(\varepsilon_1 - \varepsilon_2)v_f}{(\varepsilon_1 + 2\varepsilon_2) - (\varepsilon_1 - \varepsilon_2)v_f}\,. \tag{3.10}$$

Introducing the volume fraction β of a spherical core-shell nanostructure by

$$\beta = 1 - v_f = 1 - \left(\frac{r_1}{r_2}\right)^3, \tag{3.11}$$

the effective DF of Eq. (3.10), may be rewritten as

$$\varepsilon_I = \varepsilon_2 \frac{\varepsilon_1(3/\beta - 2) + 2\varepsilon_2}{\varepsilon_1 + \varepsilon_2(3/\beta - 1)v_f}. \tag{3.12}$$

Next, we consider an ensemble where identical spherical core-shell NPs (nano inclusions) are homogeneously dispersed in a continuous host matrix of DF, ε_h. The polarizability and effective permittivity of the system may be described by using the Clausius-Mossotti relation together with the Maxwell-Garnet mixing theory. If N denotes the density number of the inclusions in the system, then the polarizability expressed in terms of the permittivity becomes (Huang et al, 2001).

$$\frac{N\alpha}{3} = \frac{\varepsilon_{eff} - \varepsilon_h}{\varepsilon_{eff} + 2\varepsilon_h}, \tag{3.13}$$

where ε_{eff} is the effective permittivity and α is the polarizability defined by Eq. (3.9). In addition, Eq. (3.9) may conveniently be rewritten as $\alpha = 4\pi r_2^3 \eta$, where η is the dimensionless polarizability defined by

$$\eta = \frac{\varepsilon_I - \varepsilon_h}{\varepsilon_I + 2\varepsilon_h}. \tag{3.14}$$

Substituting Eq. (3.12) into (3.14) and rearranging, we find that

$$\eta = 1 - \frac{3}{2}\left[\frac{\varepsilon_2\varepsilon_3\left(\frac{3}{\beta} - 1\right) + \varepsilon_1\varepsilon_h}{\varepsilon_2^2 + \varepsilon_1\varepsilon_2\left(\frac{3}{2\beta} - 1\right) + \varepsilon_2\varepsilon_h\left(\frac{3}{\beta} - 1\right) + \varepsilon_1\varepsilon_h}\right]. \tag{3.15}$$

Furthermore, the effective permittivity of the ensemble may be obtained by substituting Eqs. (3.9) and (3.14) into Eq. (3.13). That is,

$$\varepsilon_{eff} = \varepsilon_h \left(\frac{1+2\xi\eta}{1-\xi\eta}\right) \tag{3.16}$$

Here, ξ is the filling factor of the inclusions given by

$$\xi = N\frac{4\pi r_2^3}{3}. \tag{3.17}$$

It is worthwhile to note that Eqs. (3.15) and (3.16) are general expressions for any two-layered spherical core-shell nanocomposite that are embedded in a dielectrics host matrix, regardless of whether the core-shell composites are metals, magnetic material, semiconductors, dielectrics or a combination of different more than two dissimilar materials.

The dielectric function (DF) of the Fe_3O_4 shell is chosen to be the modified Drude form that takes into account its nano-size. That is,

$$\varepsilon_2(\omega) = \varepsilon_\infty - \frac{\omega_p^2}{\omega[\omega + i\Gamma(l_e)]}, \tag{3.18}$$

where ε_∞ is the permittivity at high frequencies, ω_p is the plasma frequency, $\Gamma(l\mathrm{e})$ is the size dependent electron collision frequency, and ω is the frequency of the incident radiation. The size dependent damping parameter for shell can be expressed as (Serhan et al, 2019, Shivola, 2000, Arkhipova et al, 2015)

$$\Gamma(l_e) = \Gamma_0 + A\frac{v_F}{l_e} \tag{3.19}$$

where $\Gamma_0 = 1.06 \times 10^{14}$ rad/s is the bulk damping constant which is associated with dissipative losses, $v_F = 1.39 \times 10^6$ m/s is the velocity of electrons at the Fermi level, and A is a constant that accounts for the details of the electron scattering processes at the interfaces (Serhan et al, 2019, Shivola, 2000, Arkhipova et al, 2015). The quantity l_e is the electrons effective mean free path, which for a spherical NP of core radius r_1 and core/shell radius r_2 is given by

$$l_e = \frac{a_2}{2}\left[\left(1 - v_f^{1/3}\right)\left(1 - v_f^{2/3}\right)\right]^{1/3} \tag{3.20}$$

Further, separating Eq. (3.18) into real and imaginary, we have

$$\varepsilon_2(\omega) = \varepsilon'_2(\omega) + i\varepsilon''_2(\omega) \tag{3.21}$$

Where

$$\varepsilon'_2 = \varepsilon_\infty - \frac{1}{z^2 + p^2} \quad and \quad \varepsilon''_2 = \frac{1}{z(z^2 + \rho^2)} \tag{3.22}$$

With

$$z = \omega/\omega_p \qquad and \qquad \rho = \Gamma(l_e)/\ \omega_p$$

Polarizability

Since the permittivity (ε_2) is complex, the electric polarizability is also a complex function of the frequency ω. That is,

$$\eta = \eta' + i\eta'' \tag{3.23}$$

where η' is the real part and η'' is the imaginary part. Substituting Eq. (3.23) into (3.15), we obtain

$$\eta' = 1 - \frac{3}{2}\left[\frac{(\varepsilon'_2\Delta_1 + \varepsilon_1\varepsilon_h)\gamma + (\varepsilon''_2\Delta_1)\delta}{\gamma^2 + \delta^2}\right] \tag{3.24}$$

And

$$\eta'' = \frac{3}{2}\left[\frac{(\varepsilon'_2\Delta_1 + \varepsilon_1\varepsilon_h)\delta - (\varepsilon''_2\Delta_1)\gamma}{\gamma^2 + \delta^2}\right] \tag{3.25}$$

Where

$$\Delta_1 = \varepsilon_h\left(\frac{3}{\beta} - 1\right),$$

$$\gamma = (\varepsilon'_2)^2 - (\varepsilon''_2)^2 + \varepsilon'_2\Delta_2 + \varepsilon_1\varepsilon_h,$$

$$\delta = 2\varepsilon'_2\varepsilon''_2 + \varepsilon''_2\Delta_2,$$

$$\Delta_2 = \Delta_1 + \varepsilon_1\left(\frac{3}{2\beta} - 1\right)$$

Refractive Index

The response of a composite to an incident electromagnetic wave may be described by a complex refractive index ($\tilde{n}$), which for a nonmagnetic medium is defined by

$$\tilde{n} = \sqrt{\varepsilon_{eff}} \tag{3.26}$$

Where $\varepsilon_{eff} = \varepsilon'_{eff} + i\,\varepsilon''_{eff}$ is the complex effective DF of the composite. Introducing the real (n) and imaginary parts (k), $\tilde{n}$ may be written as

$$\tilde{n} = n + ik \tag{3.27}$$

Further, manipulating Eq. (3.26) together with ε_{eff} , we find that

$$\tilde{n}^2 = n^2 - k^2 + 2ikn = \varepsilon'_{eff} + i\varepsilon''_{eff} \tag{3.28}$$

Hence, the real and imaginary parts of the refractive index, respectively, take the form:

$$n = \frac{1}{\sqrt{2}}\left[\left(\varepsilon'^2_{eff} + \varepsilon''^2_{eff}\right)^{1/2} + \varepsilon'_{eff}\right]^{1/2} \tag{3.29}$$

$$k = \frac{1}{\sqrt{2}}\left[\left(\varepsilon'^2_{eff} + \varepsilon''^2_{eff}\right)^{1/2} - \varepsilon'_{eff}\right]^{1/2} \tag{3.30}$$

3.2 Experimental Method

3.2.1 Synthesis of Fe_3O_4 nanosheets

To the synthesis of Fe_3O_4 nanostructures, 3.97 g (0.2 M) of $FeCl_2$-$4H_2O$ and 2.78 g (0.1 M) of $FeSO_4 \cdot 7H_2O$ was added to 100 mL of deionized water under continuous stirring for 60 min to attain even dispersion. The pH value was adjust to 6.8 by using 1 M of NaOH. The solution was kept on a hot plate at 80 °C for 12 h. The final product was centrifuge and clean with deionized water and ethanol five times, then it dried at 80 °C in a hot air oven.

FIG. 3.2: The synthesized Fe_3O_4 Nanoparticles

3.2.2 Synthesis of Bi_2O_3 Nanoparticles

To prepare bismuth oxide nanoparticles, 2 g of bismuth nitrate (Merck KGaA, Germany) was dissolved in the 10 mL of deionized distilled water and continuously stirred at 90 °C. In the green synthesis, we wash herb (koseret) very well with tap water to remove waste particles. In this, 10g Bitter Clarifying (Lemon bush) herb powder was added to 100ml of distilled water and then boiled at 900C for 2hours, after it cool it was filtered by filter paper, and then we added 20 mL of aqueous Bitter Clarifying (Lemon bush) herb extract at 90 °C under constant stirring for 24 h. Bi_2O_3 NPs was prepared after 24 h at 90 °C . Then, we washed the product five times with double distilled water, and dried in a vacuum. Finally the product was heated at 550 °C in a furnace and static atmosphere of air for 5 h to ensure the removal of impurities.

FIG. 3.3: The synthesized Bi_2O_3 Nanoparticles

3.2.3 Synthesis of Fe_3O_4-Bi_2O_3 Nanocomposite

To prepare the Fe_3O_4-Bi_2O_3 nanocomposite, equal weight ratios of Fe_3O_4 and Bi_2O_3 nanostructures was added to 10 mL of deionized water under continuous ultrasonication for 3 h. The final solution was centrifuge and clean with deionized water and ethanol five times, after which it was dried in a hot air oven at 80 °C for 12 h.

FIG. 3.4: The synthesized Fe_3O_4-Bi_2O_3 Nanocomposite

Chapter Four
Result and Discussion

4.1 Numerical Analysis

For numerical evaluation, we considered an ensemble that consists of spherical Fe_3O_4 @ Bi_2O_3 core-shell quantum dots distressed in sodium dichromate (ε_h= 2.9). In the frequency domain of interest, we assumed that the DF of the Bi_2O_3 core to be a real constant that is independent of frequency (ε_1= 3.5). In addition, the DF of the Fe_3O_4 shell is chosen to be the modified Drude form that takes into account its nano-size. In this, we analyzed polarizability, refractive index and optical absorbance by varying the concentration of core and shell.

4.1.1 Polarizability

As we stated above, the permittivity (ε_2) is complex, the electric polarizability is also must be a complex function of the frequency ω. Using the above equations (3.24) and (3.25), we ploted the polarizability of the material.

Below, the real and imaginary parts of the polarizability of the Fe_3O_4@ Bi_2O_3 core-shell NPs embedded in sodium dichromate are analyzed using Eqs. (4.7) and (4.8). The parameter values used for the numerical simulations are: ε_1 = 3.5, ε_∞= 8.94, ω_p = $1.375x10^{16}$ rad/s , γ_0 = $1.06x10^{14}$ rad/s, v_F = 1.39×10^6 m/s, and A = 1

Figure 4.1, depicts the real part of the polarizability of the nano inclusions as a function of the wavelength of the incident radiation for different values of volume fraction, β. It is observed that the real part of the polarizability has two sets of resonances in the visible spectral region around λ = 430 nm and in near infrared spectral region above λ = 560 nm. The two sets of resonance peaks occur as a result of the surface plasmon resonances of Ferric oxide at the inner and outer interfaces. Due to the abundance of free carriers within the Ferric oxide shell, the set of the second resonance peaks are more pronounced than the first peaks. Moreover, when the value of β is increased, which may be realized either by decreasing the size of the core or increasing the thickness of the shell, the two resonances become closer and closer to each other indicating that the real part of the polarizability is dominated by that of the magnetic shell material.

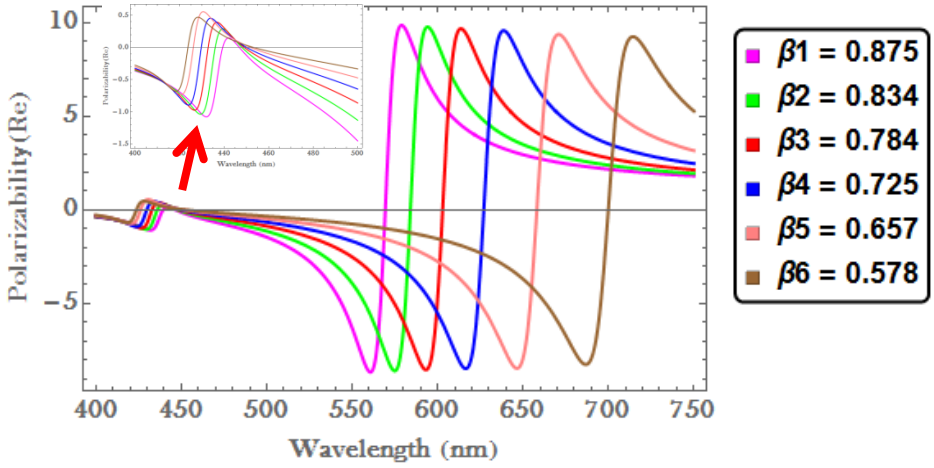

FIG. 4.1: The real part of the polarizability of the spherical nanoinclusions as a function of wavelength for different values of β.

The imaginary part of the polarizability of the nanoinclusions as a function of wavelength for different value of β is depicted in Fig. 4.2. The anomalies property is takes place at the interfaces. Similar to the previous case, two sets of resonance peaks are observed in the visible region and near infrared spectral region above λ = 550 nm. In particular, for β = 0.875, the first peak is located in the visible region at the wavelength λ = 430 nm, whereas the second resonance peak is at λ = 550 nm in infrared region. From Figs. 4.1 and 4.2, we observed that the scattering of electrons at the interface is maxima from shell surface.

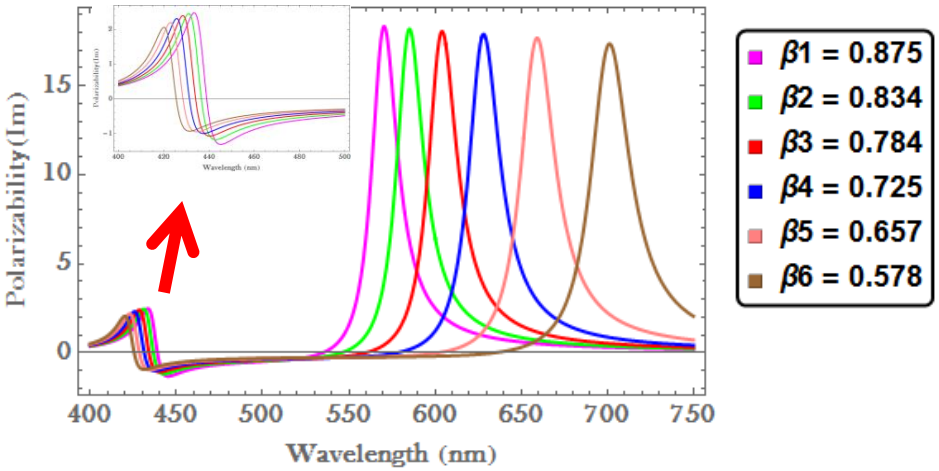

FIG. 4.2: The imaginary part of the polarizability of the nanoinclusions obtained for different values of β.

To the dielectrics Bi_2O_3 and also transmission of electrons in the Fe_3O_4 is maximum when the shell thickness is increased. Moreover, the proposed theoretical model derived via polarization in an external electric field may be valuable in controlling and designing highly absorbing electrostatic resonance and emission from nanosphere arrays particularly for hybrid photovoltaic applications. In light of the present model, we suggest that spherical core-shell nanostructure could be the optimal geometrical configuration in order to enhance optical absorbance.

4.1.2 Refractive Index

The response of a medium to an incident electromagnetic wave may be described by a complex refractive index ($\tilde{n}$), which for a nonmagnetic medium is defined by eq. (3.26).

Below, the real and imaginary parts of the refractive index of an ensemble consisting spherical Fe_3O_4@ Bi_2O_3 core-shell nano inclusions embedded in sodium dichromate are analyzed using Eqs. (4.12) and (4.13) with ε_{eff} given by Eq. (3.16). The parameter values used for the numerical evaluations are the same as that used for polarizability.

Figure 4.3, shows the real part of refractive index as a function of wavelength of the incident light for a fixed value of the filling factor ξ = 0.001 and five different values of β. The graph shows that the refractive index varies between 1.682 and 1.728 and possesses two sets of resonances corresponding to two anomalous dispersion regions; the first set in the visible region around 430 nm and the second peaks in the infrared region between 550−730 nm. The peaks show slight blue shifts in the first peak region and red shifts in the second peak region when the volume fraction, β, is increased. In addition, when β increases the two resonance peaks gets closer and closer to each other, and eventually merge for β = 1.

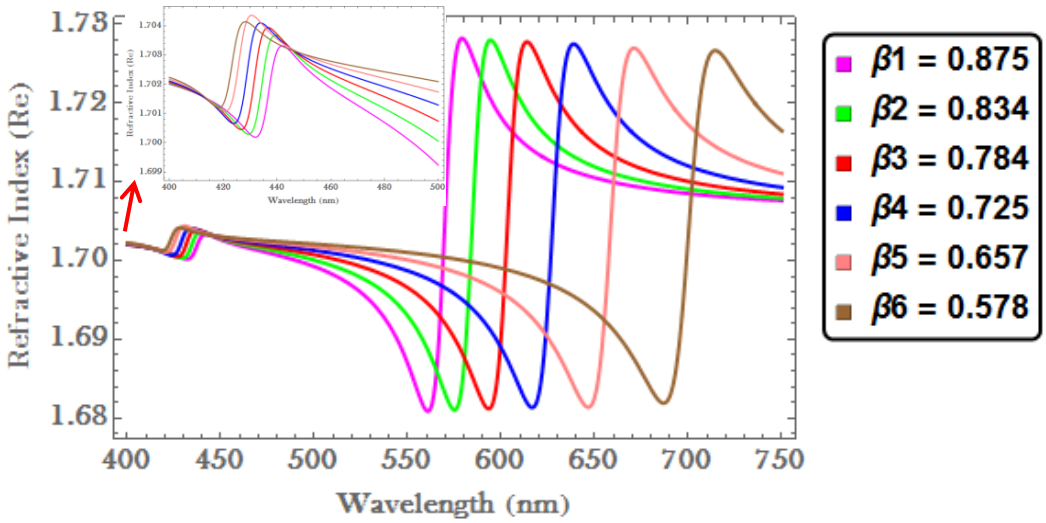

FIG. 4.3: The real part of the refractive index for fixed filling factor ξ = 0.001.

Furthermore, we analyzed the effect of varying the filling factor, ξ, on the real part of the refractive index, as shown in Fig. 4.4. It is observed that the refractive index in the vicinity of the two resonances progressively increases as ξ increases from 0.001 to 0.011 in steps of 0.002. However, the peaks position remains almost constant independent of the values of ξ. The result suggests that light propagates in the ensemble more readily when the concentration (ξ) of the nano inclusions is small. Hence, as Fig. 4.4 depicts, the refractive index near the resonances can be tuned by changing the filling factor (ξ), the shell thickness, and the density of the packed nano sphere arrays, which can play a great role in applying the core-shell structure in sensors.

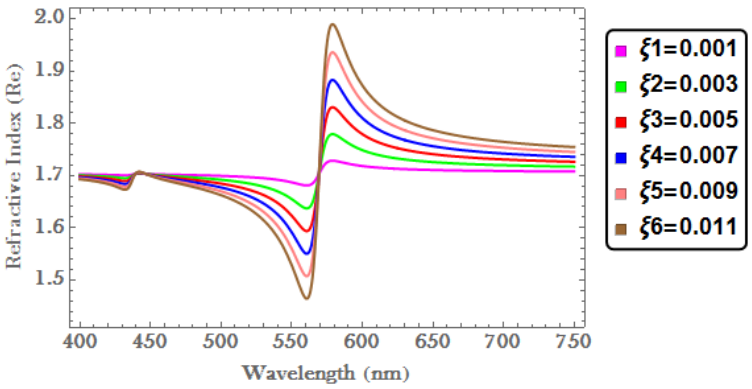

FIG. 4.4: The real part of the refractive index obtained for β = 0.875 and different values of ξ.

The imaginary part of the refractive index, shown in Fig. 4.5, has two resonances for the two anomaly dispersions of the system. When the volume fractions of the concentric spheres are nearly unity, the imaginary part of the refractive index in the 550 nm region is maximum. The positions and values of the maxima strongly depend on β (with the other parameters kept constant). In particular, for $\beta \geq 0.75$; the second maxima are about one-half smaller than the first one and the peaks are almost constant independent of β. In addition to the volume fraction, this phenomena can occur if the electric fields are comparable with the inner atomic fields. When β is increased, the peaks in the first region and second regions show blue shift and red shift, respectively.

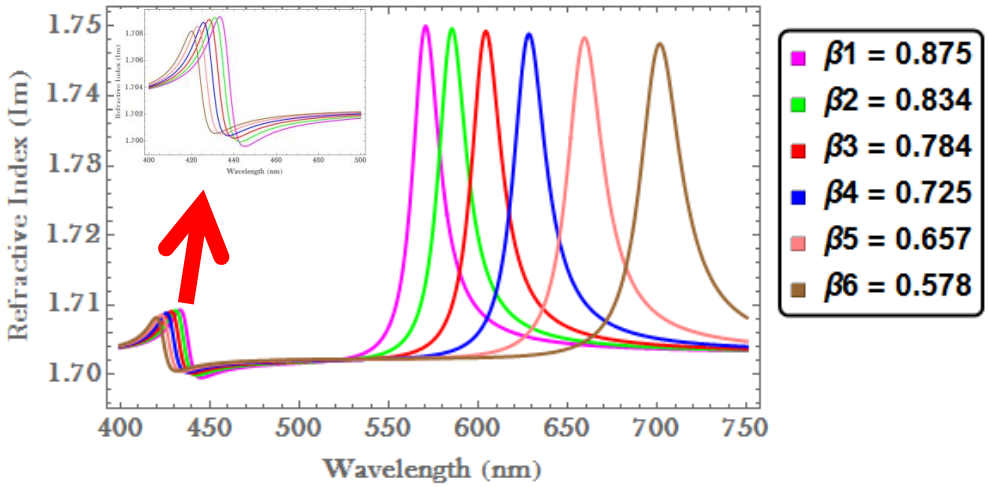

FIG. 4.5: The imaginary part of the refractive index of the spherical inclusion for fixed filling factor, $\xi = 0.001$.

4.1.3 Optical Absorbance

The spherical inclusions in the ensemble are polarizable, with field-induced dipoles, due to the interaction of the dipole moments with the applied uniform electric field. In our case, the incident field is assumed to be polarizable along the z-axis, and hence may be expressed as $E = E_0 e^{[i\omega(\tilde{n}z - ct)/c]}$, where E_0 is the amplitude of the field, $\tilde{n}$ is the complex refractive index, and c is the speed of light in vacuum. Because of the presence of the term $e^{(-k\omega z/c)}$, the wave decays as it propagates in the composite nanostructure. An incident light, in general, propagating in a medium is attenuated both by absorption and scattering (Serhan et al, 2019, Shivola, 2000, Arkhipova et al, 2015). However, for NPs that are much smaller than the wavelength of light, scattering effects may be neglected so that only the absorption contributes significantly to the attenuation. The intensity (I) of the propagating wave is related to the electric field by $I \sim |E|^2$. Generally, as the wave traverses in the medium, the intensity is attenuated as :

$$I = I_0 e^{-\alpha z} \tag{4.1}$$

Where I_0 is the intensity at z = 0 and α is the absorption coefficient defined by

$$\alpha = \frac{2k\omega}{c} = \frac{4\pi k}{\lambda}, \tag{4.2}$$

where $\lambda = 2\pi c/\omega$ is the wavelength of the incident radiation and k is the imaginary part of the refractive index. The typical length of light propagation in a material medium is represented by the absorption length *l*, which is defined by $l = 1/\alpha$. The quantity in the exponent of Eq. (4.14) is the absorbance (A) which may generally be expressed as $A = \ln(I_0/I_t) = t\alpha$, where I_t is the intensity at z = t. Thus, for the Fe_3O_4@ Bi_2O_3 nanocomposites, the absorbance at the inner interface is given by:

$$A(\lambda) = \frac{2k\omega}{c} t_{Fe_3O_4} = \frac{4\pi k}{\lambda} t_{Fe_3O_4}, \tag{4.3}$$

where $t_{Fe_3O_4} = r_2 - r_1$ is the thickness of the Fe_2O_3 shell. Figure 4.6 depicts the absorbance of the spherical Fe_3O_4@Bi_2O_3 nano inclusions as a function of wavelength for $\xi = 0.001$ and different values of β (or $t_{Fe_2O_3}$); while the core-shell radius (20 nm) is kept constant. It shows two sets of absorption peaks: the first and the second are in the visible and near infrared spectral regions, respectively.

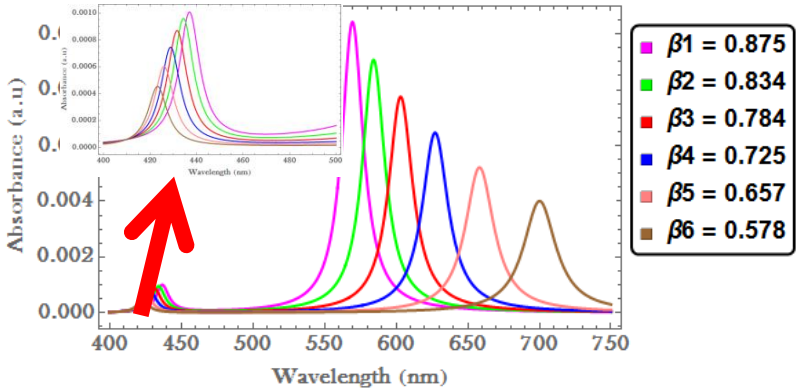

FIG. 4.6: The optical absorbance of the nano inclusions obtained for different shell thickness and fixed $\xi = 0.001$.

It is observed that when the shell thickness is increased from $t_{Fe_3O_4}$ = 5−10 nm, the resonance peaks located in the vicinity of 430 nm are enhanced and slightly blue shifted. These resonances may be attributed to near band edge absorption (NBA) due to free exciton recombination. Decreasing the size of the Bi_2O_3 core (or increasing $t_{Fe_3O_4}$) moved the absorption edge in the visible (430 nm) spectral region towards high wavelengths (red shift). The shift of the absorption edge is attributed to the change in the energy gap of the nanoparticles. It means that since the band gap of nanostructure semiconductors is increased with a decrease of their size, the so-called quantum size effect, it leads to the shift of the absorption edge towards high energy (blue shift). For a single Bi_2O_3 NP, absorption peaks originate due to the interaction between electrons in the valance band and incoming photons, which lead to the excitation of these electrons to the conduction band.

The second resonance peaks located above 550 nm are in the visible spectral region. The absorption is still enhanced when the thickness of the shell is increased. These resonance peaks are due to deep level emissions (DLE) which are attributed to the surface plasmon resonance of ferric oxide nano shell. Such absorptions in the infrared spectral region in Bi_2O_3 has been frequently ascribed to several intrinsic and extrinsic effects. The DLE or blue radiation is due to electron recombination in oxygen vacancy (V_O) with a hole in the valance band. The absorption becomes stronger as the thickness of the ferric oxide shell increases from $5 - 10$ nm. On the other hand, the resonance peaks show a red shift with an increase in shell thickness, while the broadening of the absorption spectra is observed when the thickness of the shell is decreased (Serhan et al, 2019, Shivola, 2000, Arkhipova et al, 2015). This broadening of the spectra is caused because of the incorporation of the NPs size effect in our analysis via Eq. (4.2).

It may be concluded that the direct contact between quantum dots of Bi_2O_3 and Fe_3O_4 NPs can lead to interfacial charge transfer process that are of paramount importance in highly relevant topics such as photo catalytic reactions and light energy conversion, via the application of the core-shell nanostructure.

4.2 Experimental Analysis

4.2.1 Experimental Result

4.2.1.1 Photoluminescence Result

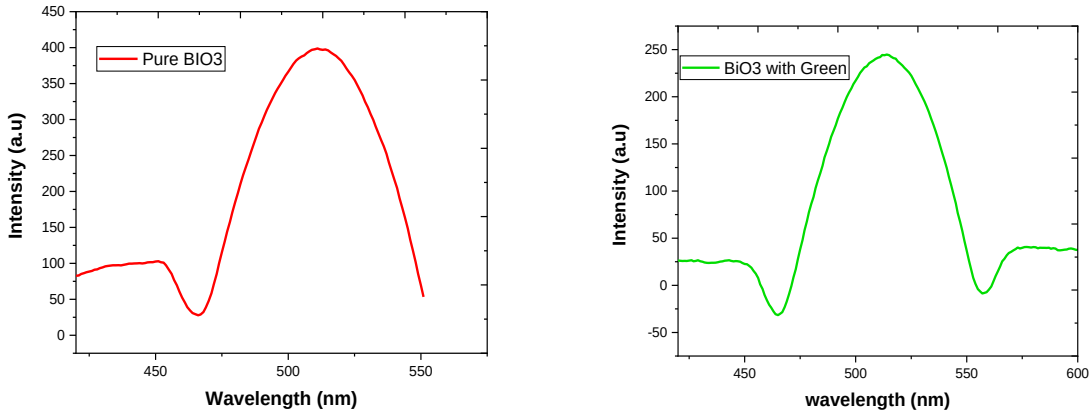

FIG 4.7: Pure Bi_2O_3 and Bi_2O_3 with herb PL result

As we see from the result the peak for pure Bi_2O_3 is obtained at 511.04nm and for Bi_2O_3 with Herb at 514.04nm, so there is small white light shift. The peak intensity of the two materials is different which means with and with green extraction affects the structure of the material. When we compare band gap also, for the pure Bi_2O_3 we obtain Eg =2.43eV and for Bi_2O_3 with Herb we obtain Eg = 2.41eV. This indicates that when we use Herb with Bi_2O_3 the Eg decreases, so the conductivity of Bi_2O_3 increases. From this result, in addition cost effective, environmental friendly and reduce chemical consumption, green synthesis route can change the morphology and properties of the material.

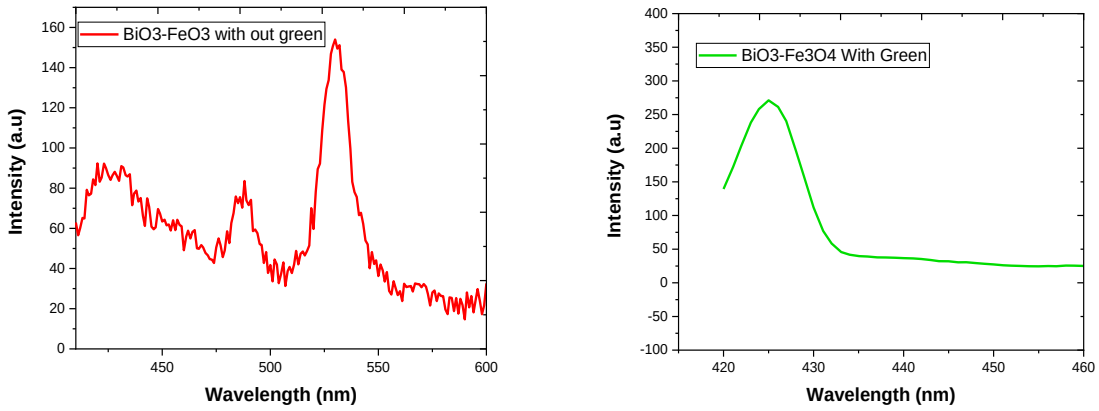

FIG 4.8: Bi_2O_3-Fe_3O4 nano composite without Herb and Bi_2O_3-Fe_3O_4 with Herb

As we see from the above graph the peak for Bi_2O_3-Fe_3O_4 without Herb is obtained at 532.94nm and for Bi_2O_3-Fe_3O_4 with Herb at 425nm, so there is a blue light shift. When we compare band gap energy for Bi2O3-Fe3O4 without Herb we obtain 2.33eV and for Bi_2O_3-Fe_3O_4 with Herb we obtain 2.32 eV. This indicates that the conductivity of Bi_2O_3-Fe_3O_4 increases when we use herb, the conductivity of Bi_2O_3-Fe_3O_4 with Herb is greater than Bi_2O_3-Fe_3O_4 without Herb. When we compare the PL result of Bi_2O_3 and Bi_2O_3-Fe_3O_4, have very related and consistency result.

4.2.2.2 XRD result

The XRD graph of pure Bi_2O_3, Bi_2O_3 with green, Fe_3O_4@Bi_2O_3 (1:1), and Fe_3O_4@Bi_2O_3 with green (1:1) nanostructures synthesized is given in Figure 4.8. As we seen from the XRD diffraction patterns, the necessary peaks are appeared in both chemical and biological synthesized samples. The peaks characteristic to the chemical synthesize Bi_2O_3 and Fe3O4@Bi_2O_3 structures were observed are relatively weak crystalized. In green synthesis of Bi_2O_3 and Fe3O4@Bi_2O_3 using herb (koseret), the crystalize structure is strong which is align with PL result. When we add green extraction solution, XRD peak intensity of Bi_2O_3 is decreased. In addition, the lack of any impurity peak in the XRD diffraction patterns in these structures indicates that they have high crystallinity. The resulting XRD patterns were seen to be consistent with the Bi_2O_3@Fe_3O_4 nanostructures obtained by different methods in the literature, but they gave better results in terms of impurity.

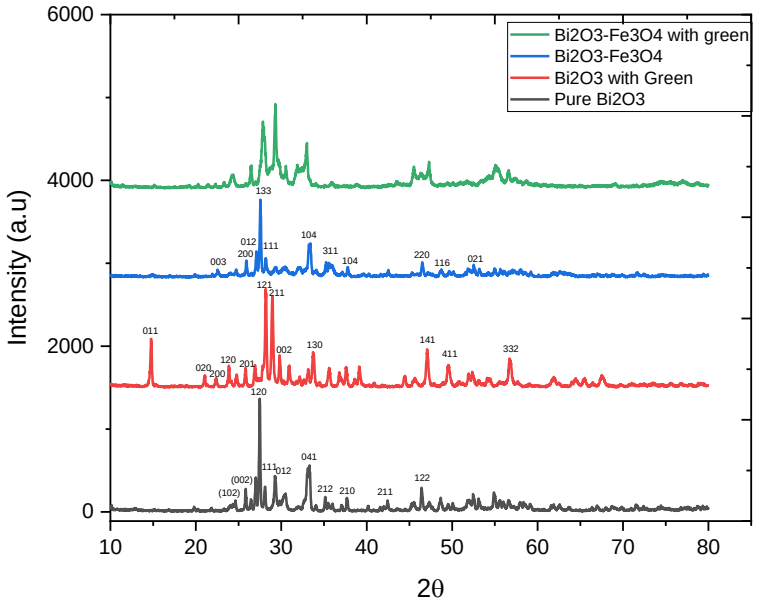

FIG.4.9: XRD result graph of Bi_2O_3 and Fe_3O_4@Bi_2O_3 .

Conclusions and Recommendations

In summary, we studied the effect of varying the core radius and thickness of the magnetic shell and semiconductor core on the optical response of nanocomposites consisting of spherical Fe_3O_4@Bi_2O_3 core-shell nanoinclusions embedded in sodium dichromate. The polarizability, refractive index, and optical absorbance of the system are determined by employing the electrostatic approximation and the Maxwell-Garnet effective medium theory. Moreover, the DF of the Fe_3O_4 shell is chosen to be of the modified Drude model form that takes into account its nano-size. It is shown that for different values of the volume fraction β and filling factors ξ, the graphs of the real and imaginary parts of the polarizability and refractive index of the nano composites as a function of wavelength possess two resonance peaks in the visible region (around 430 nm) and near infrared (between $550 - 750$ nm) spectral regions. These resonance peaks correspond to the surface plasmon resonances of Fe_2O_3 at the Bi_2O_3/Fe_3O_4 and Fe_3O_4/host-matrix interfaces, respectively. The resonance peaks show slight blue shift in the visible (430 nm) region and red shift in the infrared region above 550 nm when β or ξ is increased. Similarly, for a fixed core-shell radius of 20 nm, the graphs of the optical absorbance versus wavelength for fixed ξ = 0.001 and different values of shell thicknesses ($t_{Fe_3O_4}$ = 5−10 nm) show also two sets of absorption peaks - in the same spectral regions. It is observed that when the Fe_3O_4 shell thickness increases, the two sets of resonance peaks are enhanced; accompanied with slight blue shift in the visible (430 nm) and red shift in the infrared spectral regions above 550 nm.

The nanocomposite of Bi_2O_3 and Fe_2O_3 is experimentally investigated. The composite is studied using chemical and biological synthesis method. The green synthesis method has very fine structure than biological synthesize one. The crystality of the material is different in both. In the XRD result all peaks are appeared that shows the constituent of the composite. The band gap energy and the optical absorbance of the structure is modified when we used extracted solution. Based on the result, these materials can use for environmental remediation.

The enhancement in the optical properties is mainly attributed to strong coupling of the surface plasmon resonance of the Fe_3O_4 shell and the energy gap of the Bi_2O_3 NPs in both spectral regions. Indeed, compared with the bare Bi_2O_3, the Fe_2O_3 coated Bi_2O_3 NPs possess improved potential device applications in the optical frequency region. The results may be used to optimize 'desired' device parameters of nano composites consisting of Fe_3O_4 @Bi_2O_3 core-shell nanostructures that are designed for various applications such as sensors and nano-optoelectronics devices.

Reference

A. R. Bijanzadeh. (2012). A study of the surface plasmon absorption band for nanoparticles. *International Journal of Physical Sciences*, *7*(13). https://doi.org/10.5897/ijps11.893

Ali, A. G., Dejene, B. F., & Swart, H. C. (2016). The influence of different species of gases on the luminescent and structural properties of pulsed laser-ablated Y2O2S:Eu3+ thin films. *Applied Physics A: Materials Science and Processing*, *122*(5). https://doi.org/10.1007/s00339-016-0062-3

Bera, D., Qian, L., Tseng, T. K., & Holloway, P. H. (2010). Quantum dots and their multimodal applications: A review. In *Materials* (Vol. 3, Issue 4, pp. 2260–2345). MDPI AG. https://doi.org/10.3390/ma3042260

Beyene, G., Senbeta, T., & Mesfin, B. (2019). Size dependent optical properties of ZnO@Ag core/shell nanostructures. *Chinese Journal of Physics*, *58*(February), 235–243. https://doi.org/10.1016/j.cjph.2019.01.011

Bhardwaj, S., & Sharma, R. P. (2018). Improving range of SPR tunability and extinction efficiency of spheroidal silver nanostructures in graphene environment. *Bulletin of Materials Science*, *41*(5), 1–5. https://doi.org/10.1007/s12034-018-1637-8

Carney, P. S. (2017). Two years of tutorials: editorial. *Journal of the Optical Society of America A*, *34*(12), ED5. https://doi.org/10.1364/josaa.34.000ed5

Chavez, F. A., & Srinivasan, G. (2016). Self-assembly of nanostructures with multiferroic components using nucleic acid linkers. *MRS Communications*, *7*(1), 20–26. https://doi.org/10.1557/mrc.2016.63

Chen, L., Chen, H., & Li, Y. (2014). One-pot synthesis of Pd@MOF composites without the addition of stabilizing agents. *Chemical Communications*, *50*(94), 14752–14755. https://doi.org/10.1039/c4cc06568a

Daniel, R., & Musil, J. (2013). *Novel Nanocomposite Coatings: Advances and Industrial Applications*.

Encina, E. R., Pérez, M. A., & Coronado, E. A. (2013). Synthesis of Ag@ZnO core-shell hybrid nanostructures: An optical approach to reveal the growth mechanism. *Journal of Nanoparticle Research*, *15*(6). https://doi.org/10.1007/s11051-013-1688-0

Huang, M. H., Mao, S., Feick, H., Yan, H., Wu, Y., Kind, H., Weber, E., Russo, R., & Yang, P. (2001). Room-temperature ultraviolet nanowire nanolasers. *Science*, *292*(5523), 1897–1899. https://doi.org/10.1126/science.1060367

Ismail, A. A., Gholap, A. V., & Abbo, Y. A. (2017). Enhancement of local electric field in core-shell orientation of ellipsoidal metal/dielectric nanoparticles. *Condensed Matter Physics*, *20*(2), 1–11. https://doi.org/10.5488/CMP.20.23401

Johnson, J. C., Yan, H., Schaller, R. D., Haber, L. H., Saykally, R. J., & Yang, P. (2001). Single nanowire lasers. *Journal of Physical Chemistry B*, *105*(46), 11387–11390. https://doi.org/10.1021/jp012304t

Kalele, S., Gosavi, S. W., Urban, J., & Kulkarni, S. K. (2006). Nanoshell particles: synthesis, properties and applications. In *CURRENT SCIENCE* (Vol. 91, Issue 8).

Kaminskiene, Z., Prosyevasa, I., Stonkute, J., & Guobiene, A. (2013). Evaluation of optical properties of ag, cu, and co nanoparticles synthesized in organic medium. *Acta Physica Polonica A*, *123*(1), 111–114. https://doi.org/10.12693/APhysPolA.123.111

Lawrie, B. J., Mu, R., & Haglund, R. F. (2012). Selective Purcell enhancement of defect emission in ZnO thin films. *Optics Letters*, *37*(9), 1538. https://doi.org/10.1364/ol.37.001538

Lee, J., Shim, H. S., Lee, M., Song, J. K., & Lee, D. (2011). Size-controlled electron transfer and photocatalytic activity of ZnO-Au nanoparticle composites. *Journal of Physical Chemistry Letters*, *2*(22), 2840–2845. https://doi.org/10.1021/jz2013352

Lin, J. M., Lin, H. Y., Cheng, C. L., & Chen, Y. F. (2006). Giant enhancement of bandgap emission of ZnO nanorods by platinum nanoparticles. *Nanotechnology*, *17*(17), 4391–4394. https://doi.org/10.1088/0957-4484/17/17/017

Link, S., & El-Sayed, M. A. (2000). Shape and size dependence of radiative, non-radiative and photothermal properties of gold nanocrystals. *International Reviews in Physical Chemistry*, *19*(3), 409–453. https://doi.org/10.1080/01442350050034180

Liu, X., He, L., Zheng, J., Guo, J., Bi, F., Ma, X., Zhao, K., Liu, Y., Song, R., & Tang, Z. (2015). Solar-light-driven renewable butanol separation by core-shell Ag@ZIF-8 nanowires. *Advanced Materials*, *27*(21), 3273–3277. https://doi.org/10.1002/adma.201405583

Liu, X., Iocozzia, J., Wang, Y., Cui, X., Chen, Y., Zhao, S., Li, Z., & Lin, Z. (2017). Noble metal-metal oxide nanohybrids with tailored nanostructures for efficient solar energy conversion, photocatalysis and environmental remediation. *Energy and Environmental Science*, *10*(2), 402–434. https://doi.org/10.1039/c6ee02265k

Liu, Y., He, L., Liu, Y., Liu, J., Xiong, Y., Zheng, J., & Tang, Z. (2013). Core-shell noble-metal@metal-organic-framework nanoparticles with highly selective sensing property. *Angewandte Chemie - International Edition*, *52*(13), 3741–3745. https://doi.org/10.1002/anie.201209903

Majhi, D., Das, K., Mishra, A., Dhiman, R., & Mishra, B. G. (2020). One pot synthesis of CdS/BiOBr/Bi2O2CO3: A novel ternary double Z-scheme heterostructure photocatalyst for efficient degradation of atrazine. *Applied Catalysis B: Environmental*, *260*(1), 1–13. https://doi.org/10.1016/j.apcatb.2019.118222

McCluskey, M. D., & Jokela, S. J. (2009). Defects in ZnO. *Journal of Applied Physics*, *106*(7), 1–13. https://doi.org/10.1063/1.3216464

Mildred S. Dresselhaus. (2010). Group theory: application to condensed matter physics. In *Springer*.

Mohammed, K. A., Hadi, M. M., Al-Kabbi, A. S., & Ziadan, K. M. (2021). Effect of substrate type on the parameters of CdSe-TSC schottky diode. *Chalcogenide Letters*, *18*(7), 421–427. https://doi.org/10.15251/cl.2021.187.421

Peled, D., Pratt, V., & Holzmann, G. (1997). *Report documentation page*. *298*(0704), 405–405. https://doi.org/10.1090/dimacs/029/20

Rakkesh, R. A., & Balakumar, S. (2013). Facile synthesis of ZnO/TiO2 core-shell nanostructures and their photocatalytic activities. *Journal of Nanoscience and Nanotechnology*, *13*(1), 370–376. https://doi.org/10.1166/jnn.2013.6730

Sagadevan, S., Podder, J., & Das, I. (2017). *Recent Trends in Materials Science and Applications* (Vol. 189). http://link.springer.com/10.1007/978-3-319-44890-9

Sambou, A., Ngom, B. D., Gomis, L., & Beye, A. C. (2016). Turnability of the Plasmonic Response of the Gold Nanoparticles in Infrared Region. *American Journal of Nanomaterials*, *4*(3), 63–69. https://doi.org/10.12691/ajn-4-3-3

Serhan, M., Sprowls, M., Jackemeyer, D., Long, M., Perez, I. D., Maret, W., Tao, N., & Forzani, E. (2019). Total iron measurement in human serum with a smartphone. *AIChE Annual Meeting, Conference Proceedings*, *2019-Novem*. https://doi.org/10.1039/x0xx00000x

Shankar, R. (2017). Quantum field theory and condensed matter: An introduction. In *Quantum Field Theory and Condensed Matter: An Introduction*. https://doi.org/10.1017/9781139044349

Shen, H., Shan, C. X., Qiao, Q., Liu, J. S., Li, B. H., & Shen, D. Z. (2013). Stable surface plasmon enhanced ZnO homojunction light-emitting devices. *Journal of Materials Chemistry C*, *1*(2), 234–237. https://doi.org/10.1039/c2tc00154c

Shivola, A. (2000). Mixing rules with complex dielectric coefficients. l. Appl. 1 (4):393–415. doi: 10.1023/A:1026511515005. *Subsurf. Sens. Technol. Appl.*, *1*(4), 393–415.

Singh, S. C., Swarnkar, R. K., & Gopal, R. (2010). Zn/ZnO core/shell nanoparticles synthesized by laser ablation in aque-ous environment: Optical and structural characterizations. In *Bull. Mater. Sci* (Vol. 33, Issue 1).

Subramanian, V., Wolf, E. E., & Kamat, P. V. (2003). Green Emission to Probe Photoinduced Charging Events in ZnO-Au Nanoparticles . *J. Phys. Chem. B*, *107*(30), 7479–7485.

Wang, Z., Quan, X., Zhang, Z., & Cheng, P. (2017). *Optical Absorption of Carbon-Gold Core-Shell Nanoparticles*. 1–27.

Wolf, S., & Voshchinnikov, N. V. (2004). Mie scattering by ensembles of particles with very large size parameters. *Computer Physics Communications*, *162*(2), 113–123. https://doi.org/10.1016/j.cpc.2004.06.070

Kurnaz Yetim, N., Aslan, N., Koç, M.M.: Structural and catalytic properties of Fe3O4 doped Bi2S3 novel magnetic nanocomposites: p-Nitrophenol case. J. Environ. Chem. Eng. 8, 104258 (2020)

Aslan, N., Ceylan, B., Koç, M.M., Findik, F.: Metallic nanoparticles as X-Ray computed tomography (CT) contrast agents: a review. J. Mol. Struct. 1219, 128599 (2020)